Hyperspectral and Multispectral Image Fusion Based on Band Simulation

Xuelong Li, *Fellow, IEEE,* Yue Yuan, and Qi Wang, *Senior Member, IEEE*

Abstract—Hyperspectral image (HSI) usually has high spectral-resolution but low spatial-resolution due to hardware limitations, while multispectral image (MSI) usually has low spectral-resolution but high spatial-resolution. To obtain image with high resolution both in spectral and spatial domains, a general strategy is image fusion. A variety of methods have been proposed about this, but these methods generally cannot achieve good performance due to the incomplete overlapping wavelength of HSI and MSI. In order to solve this problem, the letter proposes a novel HSI fusion method based on band simulation. The proposed method expands MSI using spectral unmixing and acquires high-resolution image based on linear least squares. The experimental results on two hyperspectral datasets show that the proposed method outperforms the competitors, especially when the overlapping wavelength of HSI and MSI is small.

Index Terms—Image fusion, hyperspectral image (HSI), multispectral image (MSI), spectral unmixing.

I. INTRODUCTION

HYPERSPECTRAL image (HSI) is characterized by its narrow spectral range and rich bandwidth. It has many practical applications in recent years, including crop species classification, biomass and mineralogy mapping [1], cell phenotype analysis [2]. However, HSI cannot have both high spatial-resolution and high spectral-resolution due to sensor hardware limitations and the signal to noise ratio. To obtain high spatial-resolution HSI, image fusion is an effective method. It is the process of combining multiple images into a single image so as to obtain high-quality fused image. Therefore, image fusion of low resolution HSI and high resolution multispectral image (MSI), called *HS-MS fusion* [3], is taken to acquire high resolution HSI. Many different methods have been proposed for HS-MS fusion.

Methods based on the multispectral pansharpening [4]–[6] are early adopted and achieve competitive fusion performance. A framework is first proposed to solve the HS-MS fusion problem using the pansharpening algorithm: by dividing the spectral band of HSI into several regions and using traditional pan-sharpening techniques in each region [7]. The hypersharpening [8] is another framework for solving the problem. It demonstrates that the advantages of synthetic high-resolution band compared to the highest correlation high-resolution band. Although these methods can achieve the competitive fusion performance, it is still not completely suitable for HS-MS

X. Li, Y. Yuan and Q. Wang are with the School of Computer Science and with the Center for OPTical IMagery Analysis and Learning (OPTIMAL), Northwestern Polytechnical University, Xi'an 710072, China (e-mail: xuelong_li@nwpu.edu.cn; yuanyue1996@mail.nwpu.edu.cn; crabwq@gmail.com).
Q. Wang is the corresponding author.

fusion. It's easier to cause spectral distortion because the spectral dimension of HSI is much larger than MSI.

Many methods have been specially designed for HS-MS fusion. Spectral unmixing based methods use the inherent spectral properties of the scene to fuse HSI and MSI. Non-negative matrix factorization (NMF) is first used to solve the HS-MS fusion problem [9]. Then, coupled non-negative matrix factorization (CNMF) [10] uses NMF to perform alternating spectral unmixing of HSI and MSI. Similarly, to obtain the endmember matrix of HSI and the abundance matrix of MSI, Akhtar et al. [11] apply a method based on dictionary learning and sparse coding, and Lanaras et al. [12] introduce an alternate updating method using the projection gradient method. Different from matrix factorization, the tensor based HSI and MSI fusion methods have also shown their effectiveness. Dian et al. [13] propose a nonlocal sparse tensor factorization method, which decomposes the HSI into a core tensor and three dictionaries, and uses the similar HSI cubes to model the nonlocal similarities. Zhang et al. [14] tackle the fusion problem by utilizing a low-rank tensor decomposition model with a spatial-spectral-graph based regularization. In addition, Bayesian-based HS-MS fusion has also achieved good results over the last two decades. Eismann et al. [15] propose a Bayesian method based on maximum a posteriori estimation. Wei et al. [16] integrate the explicit solution of the Sylvester equation into the Bayesian HS-MS fusion method. These methods are always stable, benefiting from processing data in matrix format. However, it also makes the spectral correlation of HSI difficult to adopt.

The HS-MS fusion has been studied through deep learning in recent years [17]–[19]. The main idea of these methods is to learn the mapping between high-resolution images and low-resolution images. Though they can achieve good performance, their time cost is always expensive owing to the large size of HSI.

Due to the different wavelength ranges of HSI and MSI, in non-overlapping wavelength range, the fused image is proved to be easier to cause spectral distortion. This greatly affects the average quality of the fused image, especially when the non-overlapping wavelength range is large. In order to solve the problem, Kim et al. [20] propose a block-based fusion method with simulated band, which complements MSI in the non-overlapping wavelength range before image fusion. However, it is designed for the images which have a large area of green plant, and it does not perform well on other images.

In this letter, a novel hyperspectral and multispectral image fusion method based on band simulation, called band-simulated hyperspectral super-resolution (BSSR), is proposed.

Similar to [20], we adopt the band simulation. But the high resolution band is acquired by considering the spectral correlation of HSI. The main advantages are summarized as follows.

1) In general, hyperspectral sharpening methods directly use the original HSI and MSI. Though they can obtain good fusion results, spectral distortion is caused unavoidably. In this work, the band simulation is introduced to mitigate this problem. It produces simulated MSI which has the same wavelength range as HSI, and its effectiveness is shown in Section III-C.

2) It has been proved that a synthesized band can better sharpen HSI. Thus, we use a synthesized band to sharpen the HSI band in this work. By combining some MSI bands which similar to the corresponding HSI band, the synthesized band is used as corresponding high-resolution image.

II. METHODLOGY

In this section, the BSSR will be described in detail. First, MSI is expanded in the non-overlapping wavelength range via spectral unmixing. Then, the optimal linear combination of MSI bands is performed to obtain corresponding synthesized band for each HSI band.

A. Band Simulation

Since the fused image in the non-overlapping wavelength range is more likely to be distorted, we try to make two input images (HSI and MSI) have the same wavelength range. To do that, MSI is expanded in the non-overlapping wavelength range by adding a simulated band. In this part, spectral unmixing is adopted to obtain the expanded MSI.

Let $X = [X^1, \ldots, X^B] \in \mathbb{R}^{p \times B}$ denote the low spatial-resolution HSI, and $Y = [Y^1, \ldots, Y^b] \in \mathbb{R}^{P \times b}$ denote the high spatial-resolution MSI. Note that B and b represent the number of spectral bands, and p and P represent the number of pixels, where $b < B$ and $p < P$. Based on the linear spectral mixture model, X and Y are modeled as

$$X = WH_h + N_h \tag{1}$$

$$Y = W_m H + N_m. \tag{2}$$

Here, W and W_m are spectral signature matrices. H_h and H are abundance matrices. N_h and N_m are noise matrices. Then the approximate image ($A \in \mathbb{R}^{P \times B}$) is defined as

$$A = WH. \tag{3}$$

The approximate image A can be calculated by CNMF [10]. Now we obtain the high spatial-resolution image A, which covers the entire wavelength range of HSI.

Then, bands in non-overlapping wavelength range are selected from A, and are averaged to synthesize one band, called simulated band (S). Note that it has the same spatial resolution as MSI and contains approximate spectral information in the non-overlapping wavelength range of HSI.

Finally, the simulated band S is combined with MSI Y to form the simulated MSI (SMSI), which is denoted as $\widehat{Y} = [Y^1, \ldots, Y^b, S] \in \mathbb{R}^{P \times (b+1)}$. Note that SMSI has the same wavelength range as HSI and the same spatial resolution as MSI.

B. Image Fusion

In the previous step, we add a simulated band to the MSI, so we choose to use the band-based hypersharpening method to take advantage of the simulated band during the fusion. Thus, the regression based injection model is adopted to solve the fusion problem of HSI and SMSI. First, the detail image is introduced to increase the spatial resolution of HSI while retaining its spectral information. Before acquiring the detail image, the corresponding high spatial-resolution SMSI band ($H \in \mathbb{R}^{P \times 1}$) is obtained by the linear combination of SMSI bands. We define $V \in \mathbb{R}^{P \times (b+2)}$ and $x \in \mathbb{R}^{(b+2) \times 1}$ as:

$$V = [\widehat{Y}_d^1, \widehat{Y}_d^2, \ldots, \widehat{Y}_d^{b+1}, \mathbf{1}] \tag{4}$$

$$x = [w_1, w_2, \ldots, w_{b+1}, c]^T, \tag{5}$$

where $\widehat{Y}_d^i$ is the image that $\widehat{Y}^i$ downsampled to the same spatial resolution as HSI, w_i is the weight coefficient, and c is constant. Now, the linear combination optimal problem of SMSI bands can be expressed as

$$\min_x ||X^i - Vx||_2$$
$$s.t. \ w_k \geq 0, \quad \forall \ k, \tag{6}$$

where $||\cdot||_2$ represents the 2-norm. It indicates that the spectral information between Vx and ith band of HSI is the most redundant, so the coefficient x is the optimal linear combination coefficient of SMSI bands. That is to say, the high resolution band ($H = [\widehat{Y}^1, \widehat{Y}^2, \ldots, \widehat{Y}^{b+1}, \mathbf{1}][w_1, w_2, \ldots, w_{b+1}, c]^T$) is the most suitable to fuse with ith band of HSI. Formula (6) is a convex optimization problem [21]. To solve this problem, we use CVX, a Matlab-based modeling system for convex optimization [22].

Then the detail image ($D_i \in \mathbb{R}^{P \times 1}$) we desire can be obtained by

$$D_i = H - H_l, \tag{7}$$

where H_l is the low-pass Gaussian filter version of H.

Next, we inject the detail image into HSI so as to obtain high-resolution HSI ($Z^i \in \mathbb{R}^{P \times 1}$). The injection model is expressed by

$$Z^i = X_u^i + g_i D_i, \tag{8}$$

where X_u^i is the image that X^i upsampled to the same spatial resolution as SMSI, and g_i is the gain coefficient which is calculating by

$$g_i = \frac{\mathrm{cov}(X_u^i, H_l)}{\mathrm{cov}(H_l, H_l)}, \tag{9}$$

where $\mathrm{cov}(\cdot)$ means covariance.

Finally, by repeating the above injection process on each HSI band, the high-resolution HSI ($Z = [Z^1, \ldots, Z^B] \in \mathbb{R}^{P \times B}$) is acquired. The implementation details of BSSR are shown in Algorithm 1.

III. RESULTS

In this section, BSSR is compared with other fusion methods on different hyperspectral datasets. These comparison methods include SFIM [5] and GLP [6] based on pansharpening, ECCV'14 [11], ICCV'15 [12] and CNMF [10] based on spectral unmixing, FUSE [16] based on Bayesian, and the image fusion part of our approach (called nBSSR).

Algorithm 1 BSSR

Input: Hyperspectral image $X \in \mathbb{R}^{p \times B}$, multispectral image $Y \in \mathbb{R}^{P \times b}$.

Output: High-resolution hyperspectral image $Z \in \mathbb{R}^{P \times B}$.

    Calculate the approximate image A by (3).

    Calculate the simulated band S from A.

    Obtain the simulated multispectral images $\widehat{Y}$ by combining the simulated band S with Y.

    for $i = 1$ to B **do**

        Calculate high spatial-resolution image H by (6).

        Obtain the detail image D_i by (7).

        Obtain Z^i using the injection model (8).

    end for

A. Dataset and Settings

In order to evaluate the proposed BSSR, two different hyperspectral datasets are used: (1) HYPERSPEC-VNIR Chikusei dataset [23]; (2) HYDICE Washington, D.C., The National Mall dataset [24]. The Chikusei dataset has 128 bands in the spectral range from 363 nm to 1018 nm. The resolution of the scene is 2517×2335 pixels. In this letter, we select a subimage of 540×420 pixels, and all 128 bands. The Washington, D.C. dataset has 210 bands in the spectral range from 400 nm to 2500 nm with a scene resolution of 1280×307 pixels. In this letter, a subimage of 420×300 pixels and 191 bands is selected after removing bands which cover the water-absorbent area.

Since these hyperspectral datasets have only HSIs which are not enough for experiment, we need to acquire low spatial-resolution HSIs and high spatial-resolution MSIs. For simulating these images, we use the dataset images as reference images (R). In order to obtain low-resolution HSIs (X), the reference images are first Gaussian blurred in spatial domain, and then downsampled at a certain ratio. For two datasets, the spatial downsampling ratio is 6 and 4, respectively. As to obtain high-resolution MSIs (Y), original reference images are downsampled in spectral domain, and the spectral response function (SRF) of multispectral sensor is used as downsampling filter. The SRFs of the two multispectral sensors are used in this letter, including WV-2 and QuickBird.

The spectral overlaps of HSIs and MSIs for all two datasets are shown in Figure 1. For the Chikusei dataset, the SRF of MSI (gray area) covers substantially the entire wavelength range of HSI (yellow bars). While it covers only a small portion of the visible light wavelength range of HSI in the Washington, D.C. dataset.

B. Evaluation Metrics

In the experiments, we compare the fused image $Z = [Z^1, \ldots, Z^B] \in \mathbb{R}^{P \times B}$ with the reference image $R = [R^1, \ldots, R^B] \in \mathbb{R}^{P \times B}$ to evaluate the performance of BSSR. To evaluate the spatial quality, we adopt the peak signal to noise ratio (PSNR), which is defined as

$$\text{PSNR} = 10 \log_{10}\left(\frac{P \cdot \max(Z^i)^2}{\sum_{j=1}^{P} ||Z^i - R^i||_2^2}\right). \quad (10)$$
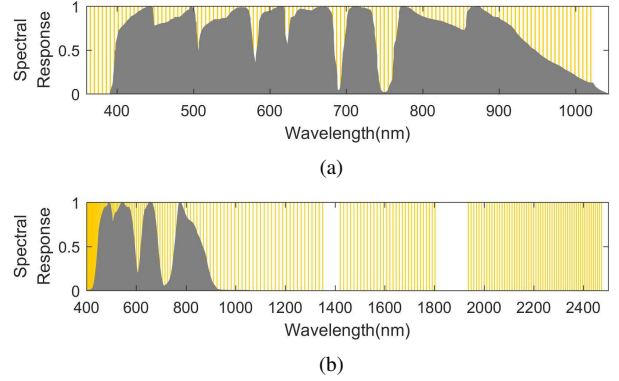

(a)

(b)

Fig. 1: The spectral overlaps of HSI and MSI on two datasets. (a) HYPERSPEC-VNIR Chikusei dataset, (b) HYDICE Washington, D.C. dataset.

To evaluate the spectral quality, we adopt the spectral angle mapping (SAM), which is defined as

$$\text{SAM} = \arccos\left(\frac{V_Z^T V_R}{||V_Z||_2 \cdot ||V_Z||_2}\right), \quad (11)$$

where V_Z is the spectral signature of a pixel in Z, and V_R is the spectral signature of a pixel in R. The Erreur relative globale adimensionnelle desynthese (ERGAS) is used for evaluating the global relative error, which is defined as

$$\text{ERGAS} = 100d\sqrt{\frac{1}{B}\sum_{i=1}^{B}\left(\frac{||Z^i - R^i||_2^2}{\frac{1}{P}\sum_{i=1}^{P} R^i}\right)^2}, \quad (12)$$

where d is the ground sample distance (GSD) ratio between MSI and HSI. The $Q2^n$ is a generalization of the general image quality index (UIQI), and it is defined as

$$\text{Q2}^{\text{n}} = \frac{4\sigma_{Z^i,R^i}\overline{Z^i} \cdot \overline{R^i}}{(\sigma_{Z^i}^2 + \sigma_{R^i}^2)(\overline{Z^i}^2 + \overline{R^i}^2)}, \quad (13)$$

where σ_{Z^i,R^i} is the covariance of Z^i and R^i. σ_{Z^i} and σ_{R^i} are the standard deviation of them, and $\overline{Z^i}$ and $\overline{R^i}$ are the mean value of them, respectively.

C. Experimental Results

The quality of the fused image is first evaluated visually. The difference image is introduced to display errors obviously, which is the difference between the fused image and the reference image in a certain band. For visually evaluated results on the Chikusei dataset, as shown in Figure 2, the two images in the first column are the low resolution HSI and the reference image at 583.4nm, respectively; the first row are the fused images; the second row are the difference images. In this figure, the fused images all get good performance compared to the reference image, while the fused image obtained by BSSR performs best. Then, the quality of the fused image is evaluated on the Washington, D.C. dataset (see Figure 3), the two images in the first column are the low resolution HSI and the reference image at 593.5nm, respectively; the first row are
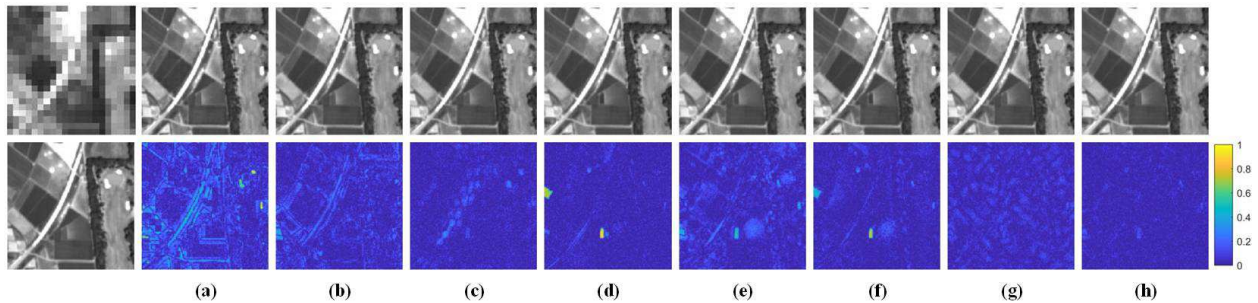
Fig. 2: HS-MS Fusion results among eight compared methods on HYPERSPEC-VNIR Chikusei dataset. (a) SFIM, (b) GLP, (c) FUSE, (d) ECCV'14, (e) ICCV'15, (f) CNMF, (g) nBSSR, (h) BSSR.
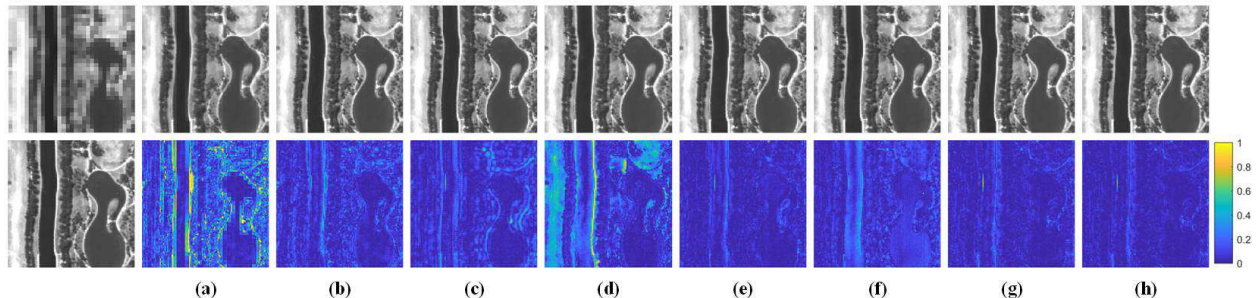

Fig. 3: HS-MS Fusion results among eight compared methods on HYDICE Washington, D.C. dataset. (a) SFIM, (b) GLP, (c) FUSE, (d) ECCV'14, (e) ICCV'15, (f) CNMF, (g) nBSSR, (h) BSSR.

TABLE I: Experimental evaluation metrics among eight compared methods on Hyperspec Chikusei dataset.

Method	Hyperspec Chikusei				
	PSNR	SAM	ERGAS	$Q2^n$	Time (s)
SFIM	43.826	1.608	1.603	0.9207	**1.06**
GLP	44.546	1.425	1.363	0.9120	14.58
FUSE	45.416	1.470	1.622	0.9198	4.75
ECCV'14	43.913	1.483	1.674	**0.9473**	1506.29
ICCV'15	42.451	1.384	1.732	0.9215	285.70
CNMF	46.132	1.245	1.542	0.9414	65.43
nBSSR	45.168	1.397	1.329	0.9467	15.38
BSSR	**46.452**	**1.178**	**1.283**	0.9424	79.83

TABLE II: Experimental evaluation metrics among eights compared methods on HYDICE Washington, D.C. dataset.

Method	HYDICE Washington, D.C.				
	PSNR	SAM	ERGAS	$Q2^n$	Time (s)
SFIM	35.544	1.950	3.333	0.8386	**0.56**
GLP	37.282	1.572	3.582	0.9086	17.90
FUSE	37.415	1.477	2.992	0.9052	3.03
ECCV'14	31.282	2.746	9.133	0.8469	587.82
ICCV'15	37.460	1.443	3.092	0.9073	186.75
CNMF	37.655	1.437	3.005	0.9113	56.52
nBSSR	38.261	**1.257**	3.152	0.9203	17.73
BSSR	**38.855**	1.261	**2.831**	**0.9227**	74.23

the fused images; the second row are the difference images. As we can observe from it, the fusion effect of ICCV'15, nBSSR and BSSR is significantly better than other algorithms, but the differences of BSSR is the smallest.

The experimental evaluation metrics of BSSR and the eight comparison algorithms on the two datasets are shown in Table I and II. Here, the bold data indicates the optimal index among the 8 groups of data. As can be seen from Table I, the fusion result without band simulation is not satisfactory, but the overall performance of BSSR is the best. The advantage of BSSR is clearly shown in Washington, D.C. dataset (Table II), which has a large non-overlapping wavelength range. In addition, though BSSR takes a little longer time than some pansharpening methods, it outperforms other algorithms.

To compare the results more intuitively, the PSNR values over HSI wavelength range are shown in Figure 4. It displays reconstruction errors of the fused images overall wavelength

range. As we can observe from this figure, BSSR has better results in non-overlapping range (the shaded regions). While in overlapping range, it shows competitive results, and it is better than other pansharpening methods. This confirms that BSSR can get better fusion performance than others especially when the overlapping wavelength range between HSI and MSI is small.

IV. CONCLUSION

In this letter, we propose a novel HSI fusion method BSSR. It focuses on improving the quality of fused image when HSI wavelength range does not coincide with MSI. Before MSI is fused with HSI, it is expanded by a spectral unmixing method to be the same wavelength range as HSI. Then, HSI is injected by the detail image of expended MSI so as to acquire high resolution HSI. Experimental results on two hyperspectral datasets indicate that BSSR can effectively improve the spatial
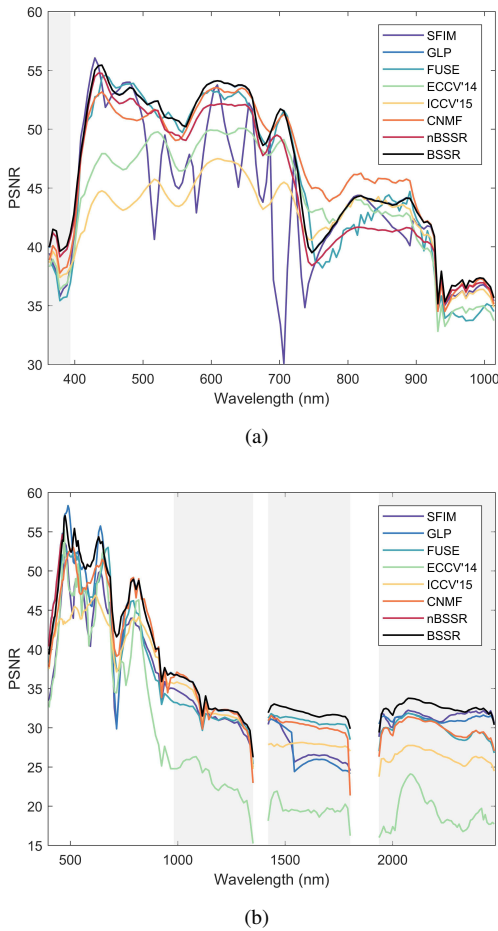
(a)

(b)

Fig. 4: PSNRs among eight compared methods on two datasets. (a) HYPERSPEC-VNIR Chikusei dataset, (b) HYDICE Washington, D.C. dataset.

resolution of HSI while preserving its spectral resolution. Aiming to acquire high resolution HSI with low hardware cost, this method makes a lot of sense. For geological applications, high resolution HSI based mineral resource detection can be more fine. Considering the number of simulated bands in BSSR is fixed to one, adaptively selecting the number of simulated bands will be our future work.

ACKNOWLEDGMENT

REFERENCES

[1] S. Boubanga-Tombet, A. Huot, I. Vitins, S. Heuberger, C. Veuve, A. Eisele, R. Hewson, E. Guyot, F. Marcotte, and M. Chamberland, "Thermal infrared hyperspectral imaging for mineralogy mapping of a mine face," *Remote Sens.*, vol. 10, no. 10, p. 1518, 2018.

[2] K. S. S. Enfield, S. D. Martin, E. A. Marshall, S. H. Y. Kung, P. Gallagher, K. Milne, Z. Chen, B. H. Nelson, S. Lam, and J. C. a. English, "Hyperspectral cell sociology reveals spatial tumor-immune cell interactions associated with lung cancer recurrence," *J. ImmunoTher. Cancer*, vol. 7, no. 1, p. 13, 2019.

[3] N. Yokoya, C. Grohnfeldt, and J. Chanussot, "Hyperspectral and multispectral data fusion: A comparative review of the recent literature," *IEEE Geosci. Remote Sens. Mag.*, vol. 5, no. 2, pp. 29–56, 2017.

[4] G. Vivone, L. Alparone, J. Chanussot, M. D. Mura, A. Garzelli, G. A. Licciardi, R. Restaino, and L. Wald, "A critical comparison among pansharpening algorithms," *IEEE Trans. Geosci. Remote Sens.*, vol. 53, no. 5, pp. 2565–2586, 2015.

[5] J. G. Liu, "Smoothing filter-based intensity modulation: A spectral preserve image fusion technique for improving spatial details," *Int. J. Remote Sens.*, vol. 21, no. 18, pp. 3461–3472, 2000.

[6] B. Aiazzi, L. Alparone, S. Baronti, A. Garzelli, and M. Selva, "MTF-tailored multiscale fusion of high-resolution MS and pan imagery," *Photogramm. Eng. Remote Sens.*, vol. 72, no. 5, pp. 591–596, 2006.

[7] Z. Chen, H. Pu, B. Wang, and G. Jiang, "Fusion of hyperspectral and multispectral images: A novel framework based on generalization of pan-sharpening methods," *IEEE Geosci. Remote Sens. Lett.*, vol. 11, no. 8, pp. 1418–1422, 2014.

[8] M. Selva, B. Aiazzi, F. Butera, L. Chiarantini, and S. Baronti, "Hypersharpening: A first approach on SIM-GA data," *IEEE J. Sel. Topics Appl. Earth Observ. Remote Sens.*, vol. 8, no. 6, pp. 3008–3024, 2015.

[9] O. Berne, A. Helens, P. Pilleri, and C. Joblin, "Non-negative matrix factorization pansharpening of hyperspectral data: An application to mid-infrared astronomy," in *2010 2nd Workshop on Hyperspectral Image and Signal Processing: Evolution in Remote Sensing*, 2010, pp. 1–4.

[10] N. Yokoya, T. Yairi, and A. Iwasaki, "Coupled non-negative matrix factorization (CNMF) for hyperspectral and multispectral data fusion: Application to pasture classification," in *Proc. IEEE Int. Geosci. Remote Sens. Symp. (IGARSS)*, 2011, pp. 1779–1782.

[11] N. Akhtar, F. Shafait, and A. Mian, "Sparse spatio-spectral representation for hyperspectral image super-resolution," in *Proc. Eur. Conf. Comput. Vis. (ECCV)*, 2014, pp. 63–78.

[12] C. Lanaras, E. Baltsavias, and K. Schindler, "Hyperspectral super-resolution by coupled spectral unmixing," in *Proc. IEEE Int. Conf. Comput. Vis.*, 2015, pp. 3586–3594.

[13] R. Dian, L. Fang, and S. Li, "Hyperspectral image super-resolution via non-local sparse tensor factorization," in *Proc. IEEE Conf. Comput. Vis. Pattern Recognit. (CVPR)*, July 2017, pp. 3862–3871.

[14] K. Zhang, M. Wang, S. Yang, and L. Jiao, "Spatial-spectral-graph-regularized low-rank tensor decomposition for multispectral and hyperspectral image fusion," *IEEE J. Sel. Topics Appl. Earth Observ. Remote Sens.*, vol. 11, no. 4, pp. 1030–1040, April 2018.

[15] M. Eismann and R. Hardie, "Application of the stochastic mixing model to hyperspectral resolution enhancement," *IEEE Trans. Geosci. Remote Sens.*, vol. 42, no. 9, pp. 1924–1933, 2004.

[16] Q. Wei, N. Dobigeon, and J.-Y. Tourneret, "Fast fusion of multi-band images based on solving a sylvester equation," *IEEE Trans. Image Process.*, vol. 24, no. 11, pp. 4109–4121, 2015.

[17] F. Palsson, J. R. Sveinsson, and M. O. Ulfarsson, "Multispectral and hyperspectral image fusion using a 3-D-convolutional neural network," *IEEE Geosci. Remote Sens. Lett.*, vol. 14, no. 5, pp. 639–643, 2017.

[18] Y. Qu, H. Qi, and C. Kwan, "Unsupervised sparse dirichlet-net for hyperspectral image super-resolution," in *Proc. IEEE Conf. Comput. Vis. Pattern Recognit. (CVPR)*, June 2018, pp. 2511–2520.

[19] R. Dian, S. Li, A. Guo, and L. Fang, "Deep hyperspectral image sharpening," *IEEE Trans. Neur. Net. Lear.*, vol. 29, no. 11, pp. 5345–5355, Nov 2018.

[20] Y. Kim, J. Choi, D. Han, and Y. Kim, "Block-based fusion algorithm with simulated band generation for hyperspectral and multispectral images of partially different wavelength ranges," *IEEE J. Sel. Topics Appl. Earth Observ. Remote Sens.*, vol. 8, no. 6, pp. 2997–3007, 2015.

[21] S. Boyd, L. Vandenberghe, and L. Faybusovich, "Convex optimization," *IEEE Trans. Autom. Control*, vol. 51, no. 11, pp. 1859–1859, 2006.

[22] M. Grant and S. Boyd, "CVX: Matlab software for disciplined convex programming, version 2.1," http://cvxr.com/cvx, Mar. 2014.

[23] N. Yokoya and A. Iwasaki, "Airborne hyperspectral data over chikusei," Space Application Laboratory, University of Tokyo, Japan, Tech. Rep. SAL-2016-05-27, May 2016. [Online]. Available: http://park.itc.u-tokyo.ac.jp/sal/hyperdata/TechRepSAL20160527.pdf

[24] M. F. Baumgardner, L. L. Biehl, and D. A. Landgrebe, *220 Band AVIRIS Hyperspectral Image Data Set: June 12, 1992 Indian Pine Test Site 3*, 2015. [Online]. Available: https://purr.purdue.edu/publications/1947/1